Miniaturisation and Evaluation of the SoftSCREEN System in Colon Phantoms

Vanni Consumi[1], *Student Member, IEEE*, Neri Niccolò Dei[2], Gastone Ciuti[2], *Senior Member, IEEE*, Danail Stoyanov[1], *Fellow, IEEE* Agostino Stilli[1], *Member, IEEE*

***Abstract*— Screening of the lower gastrointestinal (GI) tract is of paramount importance for the early detection of pre-cancerous lesions in the intestine, with an impact on reducing the high death rate of patients affected by cancer worldwide. Colonoscopy, *i.e.* standard procedure for screening the colon, is effective in reducing the incidence of colorectal cancer worldwide, nonetheless, this procedure remains an invasive method of screening, that typically causes discomfort and requires sedation for the patient. The SoftSCREEN system, a tethered robotic capsule designed for colonoscopy, aims to enable minimally invasive diagnosis of intestinal diseases through its innovative design that incorporates elastic tracks for locomotion and inflatable toroidal chambers for adaptable geometry to match the local lumen of the GI tract. After demonstrating the viability of the proposed design in a large-scale proof of concept in our previous work, the authors present here a miniaturised version of the SoftSCREEN system. We assess its performance in multiple phantom tests and evaluate the effect of pressure regulation on its locomotion. The conducted extensive tests demonstrate the capability of the soft robot to move inside intricate passages, capture internal images, and adjust its geometry to optimise traction. The results underscore the potential of the proposed design, offering promising advancements in the development of a robotic platform for efficient front-wheel locomotion and accurate intestinal screening.**

I. INTRODUCTION

The timely identification of pre-cancerous lesions in the gastrointestinal (GI) tract, such as adenomatous polyps, plays a critical role in reducing the mortality rate associated with colorectal cancer (CRC). CRC ranks as the third most commonly diagnosed cancer globally and stands as the second leading cause of cancer-related deaths [1]. The established gold standard for screening and therapeutic procedures is colonoscopy, despite drawbacks related to invasiveness and discomfort. Innovative alternative solutions are under development, emphasising minimal invasiveness through front-wheel driven solutions and mitigating issues, such as looping. Among these, robotic capsules hold significant promise [2].

This research was funded in whole, or in part, by the Wellcome/EPSRC Centre for Interventional and Surgical Sciences (WEISS) [203145/Z/16/Z]; the Department of Science, Innovation and Technology (DSIT); the Royal Academy of Engineering Chair in Emerging Technologies Scheme [CiET1819/2/36] and by the Rosetrees Trust/Stoneygate Trust Enterprise Fellowship Scheme [M884].

[1]Wellcome/EPSRC Centre for Interventional and Surgical Sciences (WEISS), University College London, London, UK vanni.consumi.20, danail.stoyanov, a.stilli@ucl.ac.uk

[2]The BioRobotics Institute & Department of Excellence in Robotics and AI, Scuola Superiore Sant'Anna, Pisa, Italy neriniccolo.dei, gastone.ciuti@santannapisa.it

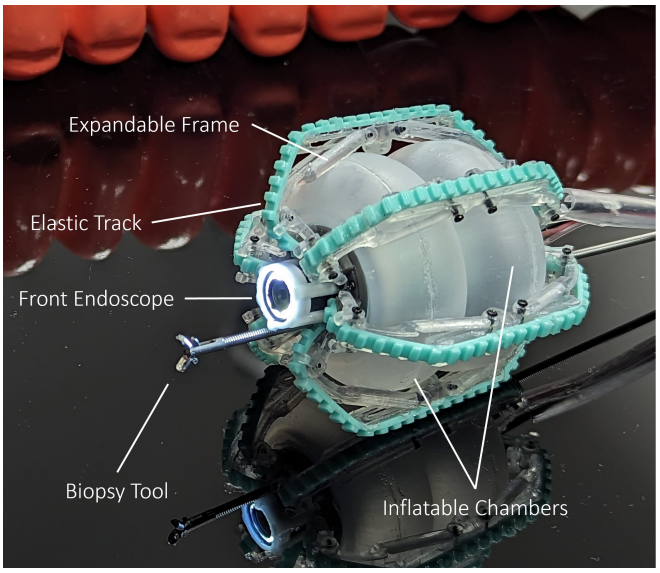

Fig. 1: The SoftSCREEN robot: main components are the central chassis, to which two inflatable chambers for shape reconfigurability are installed. These expand to put elastic tracks in contact with the colon mucosa, while stabilised by a rigid, expandable frame. A front-facing endoscope is installed in the main chassis for image recording.

Nevertheless, the development of robotic capsules presents several engineering challenges due to the frictional condition, tortuosity and limited size of the intestine [3]. Various design approaches have been explored to enable front-wheel locomotion of tethered robotic endoscopes [4][5]. One of the leading approaches in the field is represented by magnetic-assisted robotic endoscopy, wherein the robots are moved by the drag of an external permanent magnet [6], controlled with a robotic arm to enable dexterity and autonomy [7] [8] [9], or by an external rotating electromagnetic field, such as in the design of a vibro-impact robot [10]. A different design approach is the integration of small on-board electric motors, typically 6mm in diameter, inside miniature robots as reported in [11], [12], [13], [14], or the use of single external motor and a flexible shaft such as in [15], [16] and [17]. In particular, the track-driven system designed by Lee *et al.* could adapt to the size of the lumen only passively by mean of flexible tracks, and when tested on live pigs, it encountered various challenges, as the robot was unable to reach the cecum and instead came to a halt at the distal transverse colon [17]. This further proves that the capability to actively adjust the shape of the robot and its interaction with the intestinal lumen is a crucial factor for generating efficient

locomotion and stability. In this context, the employment of soft inflatable chambers offers an effective method to achieve volumetric expansion with limited space occupancy. With application in colonoscopy, the use of inflatable balloons is reported for sensing in [18], to yield augmented traction in [13], and for the locomotion mode of inch-worm in robots such as [19]. Notably, aligning the central axis of the robot with that of the lumen allows optimal positioning of the camera within the centre, thereby enhancing internal imaging and providing better guidance to the clinician during navigation. As for many of the existing robotic solutions designed for GI interventions, it is important to note that performing surgical procedures beyond screening often involves the necessity of a trailing tether for tool passage, that may incorporate electrical, pneumatic, or hydraulic lines for the actuation of the robot. As the robot progresses through the navigated GI tract, the frictional resistance caused by the movement of this tether against the intestinal walls increases. In a study conducted by Ortega *et al.* [20] the pulling force required at the tip of the endoscope to fully intubate the cecum was found to surpass 2 N due to this tether-associated resistance. In our previous research, we introduced a novel design for a reconfigurable soft robotic system for colonoscopy named SoftSCREEN and we presented a large-scale proof of concept prototype [21]. The SoftSCREEN system leverages track-based propulsion in combination with a shape-shifting design enabled by two inflatable toroidal chambers. These chambers are capable of displacing a series of six elastic tracks distributed on the external surface of the robot, ensuring their contact with the contours of the local lumen, thus enabling full-body track locomotion. Our seminal work laid the foundation by validating this design through a large-scale system and our findings showcased the feasibility of adjusting the diameter of the system to match the shape of the navigated lumen and also the capacity to regulate the force exerted on the walls through pressure regulation. As a result, we were able to modulate the traction force of our system effectively. In this study, we present a miniaturised prototype of the SoftSCREEN system and we assess its locomotion performance inside intestine phantoms.

II. LOCOMOTION MODELLING

In this study, the miniaturised system we present is an evolution of the design concept originally introduced by the authors in [21], as illustrated in Fig. 1. The system incorporates two inflatable chambers, which enable it to adapt to the various anatomical differences found within the GI tract, so to exert a wall-pressing action on the outer lining to effectively control traction, as depicted in Fig. 2-A. The ideal condition for the track-based locomotion consists of no slippage occuring between the portion of track in contact and the colon mucosa. This entails limited risks of lacerations and damage on the tissue, as well as it implies a static friction at the contact. Under this condition, the velocity of the robot depends on the rotational speed of the internal motor ω and the pitch of the worm gear p, as illustrated in Fig. 2-B.:

$$v_r = \frac{\omega p}{2\pi} \tag{1}$$

The tangential force of the worm gear F_{tng} is determined by the pitch diameter of the worm D_W and the motor torque τ_M, which is a function of the current drawn I, the torque constant K_M, the gearbox ratio r and efficiency η of the gearbox:

$$F_{tng} = \frac{2\tau_M}{D_W} = \frac{2K_M I r \eta}{D_W} \tag{2}$$

As shown in Fig. 2-B, the forces transmitted by the worm gear to the track can be defined in terms of axial force F_{ax} and tangential force F_{tng} as follows (considering that the normal pressure angle of the worm gear is zero):

$$F_{tng} = R\sin\theta + \mu_{int} R\cos\theta \tag{3}$$

$$F_{ax} = R\cos\theta - \mu_{int} R\sin\theta \tag{4}$$

where R denotes the reacting force normal to the worm tooth, μ_{int} denotes the kinetic friction coefficient between tracks and worm gear, and θ is the lead angle of the worm gear. Consequently, the axial force on the tracks is a function of the motor current drawn:

$$F_{ax} = \frac{2K_M I r \eta(\cos\theta - \mu_{int}\sin\theta)}{D(\sin\theta + \mu_{int}\cos\theta)} \tag{5}$$

As depicted in Fig. 2-C, the robot experiences various forces while moving through the GI tract. These external forces encompass gravity, buoyancy, fluid drag, cable resistance, intra-abdominal pressure, and environmental pressure, as summarised in [2].

The normal force denoted as N, which acts on the tracks of the system, is a consequence of the localised contact pressure exerted by the colon on the outer surface of the robot. This pressure results from both the intra-abdominal pressure and the environmental pressure due to the presence of the robot, as modelled in [22] and [23].

The propelling force of the system originates from the contact between the tracks and the robot as they loop around the chassis (referred to as force 4 in Fig. 2-C). The internal sliding resistance, denoted as $F_F(D, N)$, depends on both the tension in the track and the external force applied to the tracks: an increase in the diameter D of the robot can elevate track tension, then the resulting contact pressure on the tracks against the chassis and worm gear increases the sliding friction; similarly when the tracks are in contact with the surrounding wall, the external force N acts perpendicular to the tracks and elevate the friction. External sources of resistance include the contact friction with the surroundings, referred to as F_{cont}, such as the portion of the inflated chamber between two consecutive tracks that may touch the intestinal fold, the viscous friction due to the presence of liquid, named F_{visc}, and the drag force of the tether, named F_{cable}. Therefore, if the robot moves at a constant speed, the axial force must be equal to the resistance acting on the system:

$$F_{ax} = F_F(D, N) + F_{cont} + F_{visc} + F_{cable} \tag{6}$$

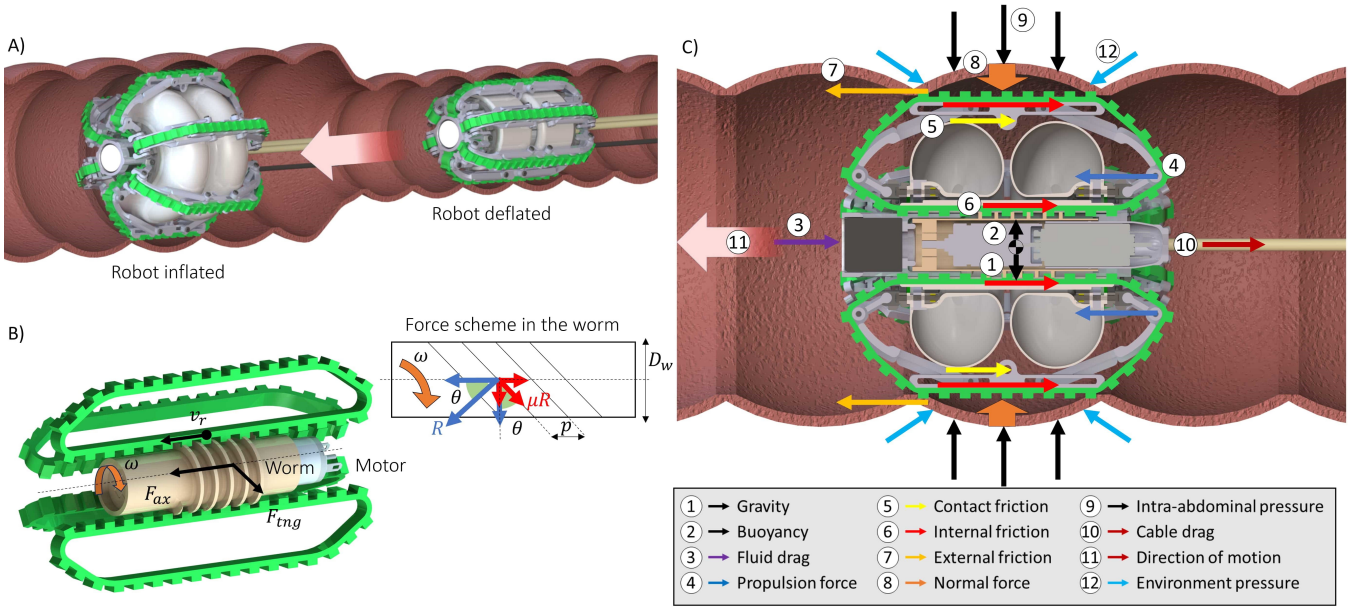

Fig. 2: A) Representation of the system inside the colon in the non-inflated configuration (left) and inflated configuration (right). B) View and scheme of the forces of the internal worm mechanism. C) Section view of the system in the inflated configuration and representation of the main forces in action during the locomotion of the robot.

The maximum propulsion force achievable equals the friction force at the contact between the tracks and the colon wall (force 7 in Fig. 2-C). Considering static friction, the increment of the diameter of the robot results in a higher normal reaction N with the intestinal wall:

$$F_{o,max} = \mu_{ext} N \tag{7}$$

where μ_{ext} is the static frictional coefficient between the tracks and the wall of the intestine. Therefore:

$$F_{ax} \leq F_{o,max} \tag{8}$$

III. DESIGN AND CONTROL

This section presents the design of the robot, whose size at the proposed state is ϕ35mm×60mm.

As displayed in Fig. 3-A and 3-B, within a cylindrical chassis of ϕ16.9mm, the robot houses a ϕ8mm DC electric motor (347727, Maxon Motor™, Sashseln, Switzerland) paired with a 256:1 reduction gear (468996, Maxon Motor™), and connected to the worm gear via a metal shaft coupling (both custom). A full-HD endoscope (Misumi Electronics Corp., Taiwan), equipped with integrated illumination, is integrated at the front, enabling visual imaging of the luminal interior. Moreover, a dedicated pathway for the passage of a ϕ2.3mm biopsy forceps, accessible from the rear side, is incorporated in the robot. The rigid parts of the system are 3D-printed via a Formlabs™ 3D printer (Somerville, MA, US) in Clear Resin, while silicone parts were cast using silicone injection inside 3D-printed molds.

A. Design of the tracks

The design of the six tracks, symmetrically spaced with an interval of 60 degrees around the circumference of the robot, has a major impact on its propulsion. The external facet of the tracks is designed to provide a high frictional interface with the intestinal wall, while the internal facet slides on the internal cylindrical surface within the chassis that houses the worm gear. As such, to ensure high efficiency in the mechanical transmission between the worm gear and the tracks, the flat internal facet needs to offer minimal sliding friction. As a result, the track features 1-mm high teeth on the external side for optimised external friction on the tooth head and robust engagement with the worm gear, while the internal side, a 1 mm thick base, has a smooth surface to reduce internal friction. The maximum width w to accommodate n tracks is calculated by inscribing an n-sided equilateral polygon within a circumference with a radius equal to the pitch radius of the worm gear, as represented in Fig. 3-A:

$$w = D_W \sin \frac{\pi}{n} \tag{9}$$

The actual width of the track that engages with the worm gear results to be lower than that, as we accounted for the longitudinal gap between the tracks to be reserved for tools, endoscope cables, and the air channels servicing the inflatable chambers; the resulting width is 3 mm, the pitch of the track p and pitch angle θ are 3 mm and 5.5 degrees respectively. A Shore 60 A hardness silicone material (Smooth-Sil 960™, Smooth-On Inc., Macungie, PA, US) is chosen for the tracks to provide effective power transmission and the required level of elasticity. Each track is manufactured straight, then it is looped around the chassis, and its extremities are bonded with Sil-Poxy adhesive from the same brand. The worm gear teeth are designed with the same pitch angle as the tracks, while the pitch diameter of the worm gear (D_W) is 9.8mm.

B. Inflatable chamber design

The inflatable chamber of our system is designed as the one previously adopted in [21] and consists of a 1 mm thick and ϕ26.6 mm external diameter membrane made of Dragon

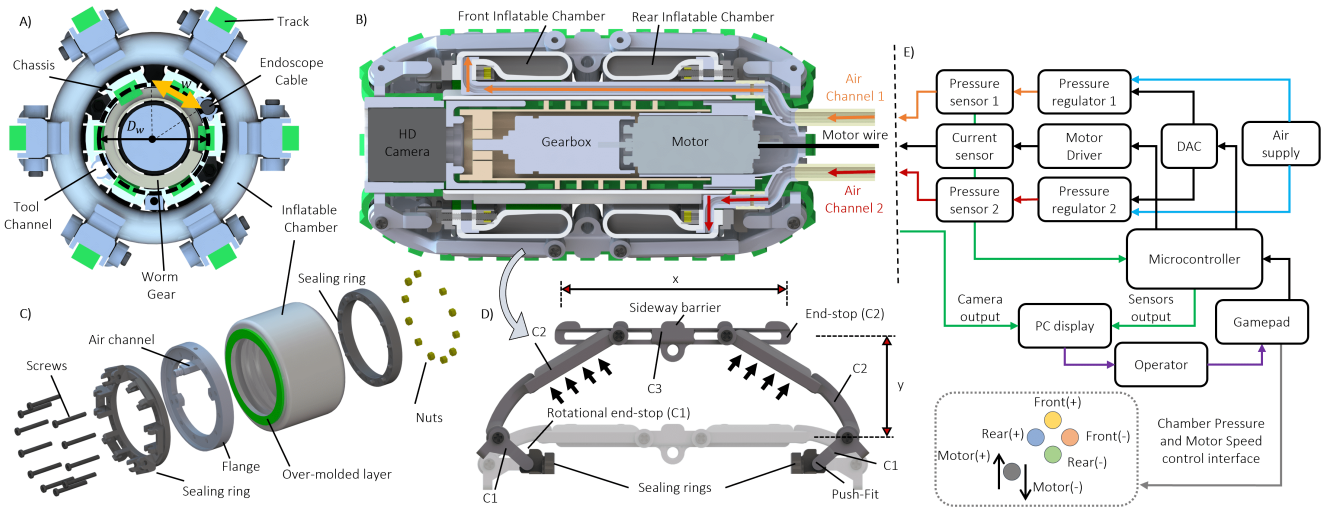

Fig. 3: A) Cross section of the robot, showing the arrangement of the tracks around the worm gear internally. The longitudinal space between two adjacent tracks is employed to allocate air channels, the camera cable, and the tool port. B) Longitudinal section of the robot, showing the connection of the two inflatable modules to the chassis, and the internal air channels rooted inside the robot to reach the rear side of the robot. The back part houses the motor and includes air channels connected to the external air supply. C) Exploded view of the inflatable chamber module. D) Picture of the expandable mechanism in the closed (transparent) and open layout. The upper component C3 provides the wall-pressing action and ensures traction. E) Control scheme of the robot. The blue lines represent the high-pressure line, the orange and red lines are the front chamber pressure and rear chamber pressure lines respectively, the black lines are the electric connections, the green lines represent the feedback signals, and the purple lines represent the actions of the operator.

Skin™ 10 NV silicone (Smooth-On Inc., Easton, PA, US). External air is introduced into the chambers from the rear of the robot, via air channels that span along the length of the robot, between adjacent tracks, as shown in Fig. 3-B. The chamber is designed with two flanges that are mounted to a rigid flange embedding the air channel. The airtight fastening is ensured by two sealing rings, secured via screws passing from one side of the flange to the other, as shown in Fig. 3-C. Since the screws pierce through the membrane, the front flange of each chamber is reinforced with an over-molded layer of hard silicone (Smooth-Sil 960™) to prevent the risk of tearing upon inflation. This dual-layered design approach enables robust fixation while maintaining highly deformable material for the rest of the body.

C. Deployable structure design

The robot also incorporates a deployable structure, similar to the one described in our previous work [21]. This structure deploys passively when the chambers inflate, allowing reconfiguration of the terminal sides of the robot, and it retracts when the chambers deflate, both for the elastic retraction of the tracks and for the interaction with the intestinal wall (being an underactuated frame). The mechanism consists of five components, labeled C1 (two components), C2 (two components), and C3 (one component), interconnected through M1 screws that act as planar hinges (see Fig. 3-D): C3 is designed so that the two components C2 are connected to it as carriages, embedding end-stops for the stroke of C2, and the frame is mounted with a push-fit connection of C1 on the sealing rings of the chambers. As the chambers inflate, the C2 component pushes up and deploys C3 along the $y > 0$ axis, ultimately bringing the tracks into contact with the external wall. The deployable mechanism aims to prevent unintended sideways motion of the tracks when it is in contact with the external wall, which would impede the correct locomotion of the robot, by mean of small side barriers designed on C3. Moreover, the deployable frame is mounted after the assembly of the tracks, so that it confers an initial pre-tension to the track to maintain the intended path-lane. Furthermore, C3 serves to maintain a consistent minimum number i of track teeth in contact with the external wall, $i = x/p$, where x is the length of C3 (35 mm) and p represents the track pitch. Finally, it reduces the possibility of the chambers contacting the intestinal wall, as the tracks are separated from the chambers by the height of C3 (3 mm), as illustrated in Fig. 3-A. The maximum vertical deployment y achievable from the initial configuration (Fig. 3-D) is circa 27.4 mm, and it is function of the length of the links and the location of the end-stops on C3.

D. Control system

The robot is controlled in open-loop, with direct management of the pressure of the chambers and of the motor speed by the operator. The user can assess the state of the motion of the robot by visualising the image output of the endoscopic camera on a laptop screen and can adjust the chamber pressure to modulate the traction accordingly. The control scheme is displayed in Fig 3-E. The two chambers are actuated pneumatically via pressure regulators (VPPX-6F-L-1-F-0L10H-S1, FESTO GmbH, Esslingen, Germany), connected to a DAC (DA4C010BI, APTINEX Ltd., Maharagama, Sri Lanka). The DC motor is driven by a motor driver (DRV8876, Pololu, Las Vegas, NV, US), and a current sensor (INA219, Adafruit Industries, NY, US) is used to evaluate the current drawn in the motor. The overall control is handled by an STM32 Nucleo-64 microcontroller (STMicroelectronics, Geneva, Switzerland), and the user interfaces the robot with a gamepad controller:

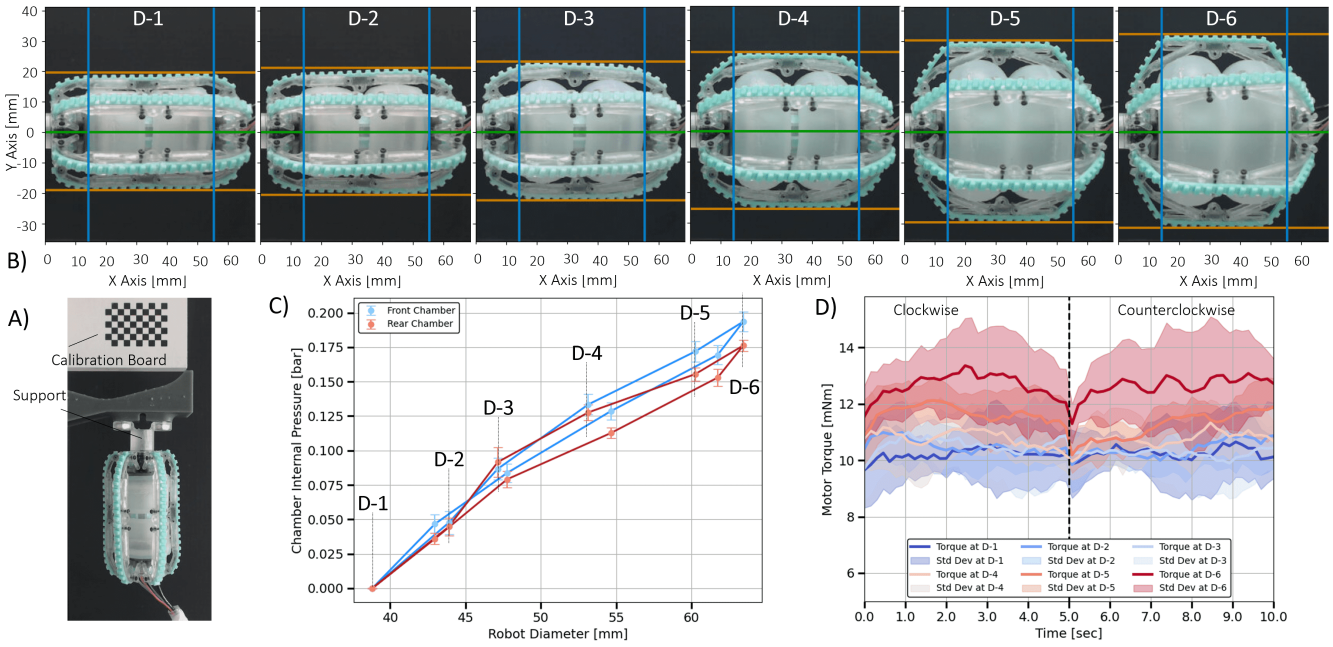

Fig. 4: A) Setup for the static measurement of the maximum diameter and the torque of the robot, with the support and the calibration board. B) Pictures of six deformation points of the inflation of the robot. Pictures are used to calibrate the robot's diameter over the internal chamber pressure and to assess the variation of the motor torque required at different levels of inflation. C) The pressure-diameter characteristic curve for the two inflatable chambers of the system, measured over five cycles of inflation and deflation of the robot. The points named from D-1 to D-6 represent the inflation phase of the cycle. D) Plot of the motor torque measured at the different robot's diameters (from D-1 to D-6), when moving the tracks forward and backward. The solid line represents the mean value of the torque of five experiments, the shaded area represents the standard deviation.

the quartet of right-hand side buttons on the gamepad is used to manipulate the voltage of the pressure regulators, to increase or reduce the pressure inside the chambers, while the right thumbstick of the joystick, used as a 2-axis controller, is dedicated to controlling the motor voltage, enabling clockwise or counterclockwise motor rotation. The kinematics of the center of the robot is primarily determined by Eq. (1), assuming static contact of the tracks with the outer wall. In practice, the flexures and the slippery walls of the intestine can result in a reduction of the overall speed of the robot.

IV. RESULTS

E. The Shape-Shifting capability

This section assesses the shape-shifting capability of our system and examines its effect on the motor torque requirement in a scenario without external walls. We established the relationship between the maximum diameter of the robot and the internal pressure applied in the chamber, used for the shape change, as well as the relationship between the diameter and motion efficiency. As the contact pressure between the rigid frame of the robot and the tracks varies depending on the diameter of the chambers, the resulting friction is reflected in the torque required by the motor to actuate the tracks.

The method for the measurement is the following. The robot is placed on a static setup where it is held at the front and elevated from the ground, thereby inflated without surrounding walls, as shown in Fig. 4-A. Five cycles (each composed of an inflation and a deflation phase) are considered to observe for repeatability and the presence of hysteresis in the silicone chamber. Each cycle has been arbitrarily divided into ten consecutive deformation steps at which the diameter of the robot and the pressure in the chambers are measured. For each step, an image is captured from a static camera (C922, Logitech, Switzerland) and the maximum diameter is obtained by measuring the distance between two opposite tracks using color segmentation of the images. For each inflation phase, that is the first six deformation steps of each experiment (from D-1 to D-6) as illustrated in Fig. 4-B, the tracks are actuated for 10 seconds (5 seconds forward and 5 seconds backward), and the current drawn by the motor is recorded. Thereafter, the magnitude of motor torque τ_M was derived from Eq.(2) using K_M (7.11 mNm/A) and η (0.65) from datasheet. The values of current and pressures are sampled at 8.6 Hz, and processed with a rolling mean calculation over ten consecutive time steps, considering the two direction of motion of the track (clockwise and counterclockwise) separately.

The resulting pressure-diameter characteristic curve for all the experiments, for both the front and rear chambers (Fig. 4-C), shows the robot can reach over 60mm in diameter, with an average peak internal pressure of 0.179 bar for the front chamber and 0.167 bar for the rear chamber. For each cycle, slight discrepancy in the internal pressure of the chambers and hysteresis were observed. We assume this is due to the differences in manufacturing and assemblying the two chambers, while for the hysteresis, it is due to the property of the material used. In Fig. 4-D, the estimation of the required torque is reported expressed as mean value and standard deviation, revealing that it increased by 38%, from 9.65 to

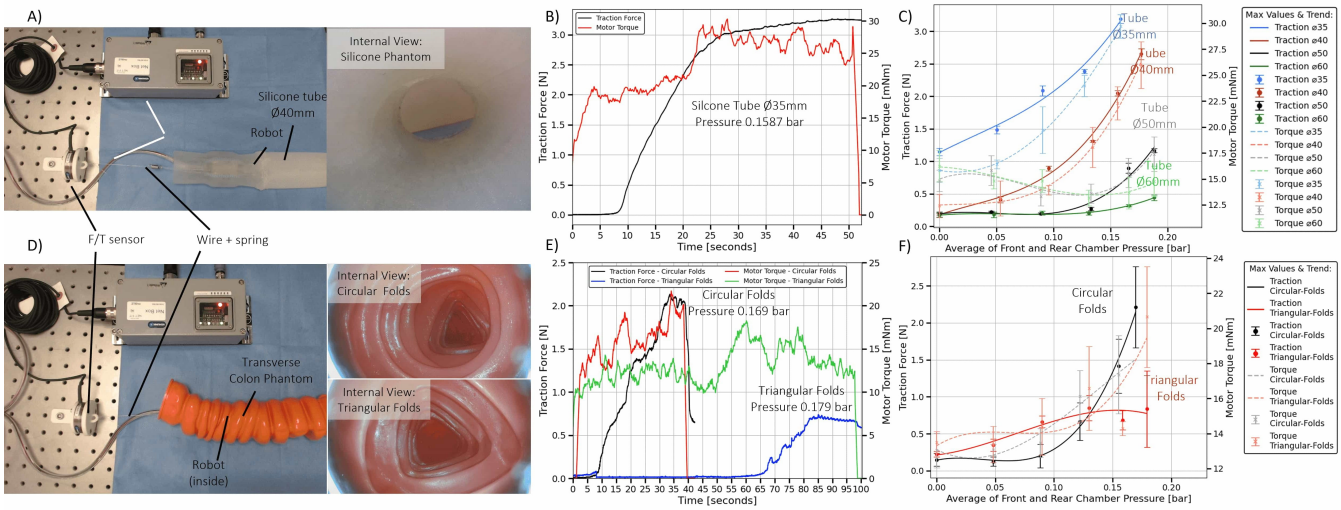

Fig. 5: A) Experimental setup for the evaluation of the maximum pulling force inside a set of four silicone tubes of different internal diameters. The internal view from the robot endoscope shows the circular internal profile of the silicone tube (no folds). B) Results for pulling force and motor torque during a test inside the ø35mm tube and a chamber pressure of 0.1587 (as averaged between the front and rear chamber pressure). Data reported have been processed with a rolling mean over ten consecutive time steps. C) Mean values (of five tests) for maximum traction force (dots) and maximum motor torque (crosses), evaluated at different internal pressure chambers inside silicone tubes of ø35mm, ø40mm, ø50mm, and ø60 mm internal diameter. The mean values are fitted with a polynomial curve (solid lines for the traction and dashed lines for the torque). All the mean values are presented with a standard deviation of five tests executed for each pressures. D) Experimental setup for the evaluation of the maximum pulling force inside the transverse colon simulator. The internal view from the robot endoscope shows the different profiles of colon folds (circular and triangular) located in the transverse. E) Results for pulling force and motor torque during a test inside the region of circular folds and the region of triangular folds, chamber pressure of the test displayed are 0.169 bar and 0.179 bar respectively (as averaged between the front and rear chamber pressure). Data reported have been processed with a rolling mean over ten consecutive time steps. F) Mean values (of five tests) for maximum traction force (dots) and maximum motor torque (crosses), evaluated at different internal pressure chambers inside both the segments with circular and triangular-shaped folds. The mean values are fitted with a polynomial curve (solid lines for the traction and dashed lines for the torque). All the mean values are presented with a standard deviation of five tests executed for each pressures.

13.35 mNm, when the robot transitioned from the non-inflated to the maximum inflated state. These findings confirm the dependency of the internal friction $F_f(D, N)$ on the robot's diameter D. Nevertheless, the expandable mechanism entails limited torque demand and facilitates tracks motion.

F. Characterisation of the Traction

The enhancement of traction as a result of the inflation of the silicone chamber is characterised inside various lumen diameters found in the GI tract. To derive the maximum force for movement based on different pressures, we measured the pulling force of the robot inside custom straight circular tubes with an internal diameter of ø35mm, ø40mm, ø50mm and ø60mm, 2 mm of thickness and 290 mm in length, manufactured with EcoFlex™ 00-50 silicone (Smooth-On), as well as inside the commercial colonoscopy simulator (Type II LM-107, KOKEN CO., LTD., Tokyo, Japan). The range of internal chamber pressures obtained from the previous static measurement was employed as input pressure for this experiment (pressures measured for the points from D-1 to D-6 of Fig. 4-B, except for the traction inside the custom ø35mm silicone tube, that was measured up to the pressure in D-5 to avoid damage to the tracks due to over-pressurisation). The experimental setup used is illustrated in Fig. 5-A. The back of the robot is connected to a force sensor (Nano43, ATI Industrial Automation, Apex, NC 27539 USA) using a non-extendable wire and a spring and the traction is measured throughout the initial 150 mm from the conduit's entrance (where five grams of Vaseline were applied to mimic the frictional condition of the intestine), while the opposite side of the tube is secured to the table with screws. For each pressure level, five pulling tests were performed: as reported in Fig. 5-B, as the robot progresses through the tube, the exerted force steadily increases until it reaches a peak, causing the spring to undergo extension. Subsequently, the force levels off, signaling the completion of the test. Force measurements (sampled at 500 Hz), current, and pressure (both at 8.6 Hz) were processed with a rolling mean over ten consecutive time steps for the analysis. For all the silicone tubes evaluated, the results of the maximum traction force and maximum motor torque are represented in Fig. 5-C and illustrate a significant increase in the traction force of the robot as a direct result of increasing the internal pressure of the inflatable chambers. Once the diameters of robot and tube matched, further increment of the pressure increased the traction. The maximum pulling force measured in all four diameters rises with increased internal chamber pressure, with higher values for smaller lumen diameter and lower overall as the diameter of the tube increases. For the case of a ø35mm tube, the traction force ultimately exceeds 3 N. Similarly, higher propulsion forces were deployed by a higher motor torque, with a maximum of 29.69 mNm. The magnification of the traction in the case of a ø60mm tube was minimal because the robot enlarged its diameter up to the lumen diameter but did not apply extensive contact force to the internal surface. Inside the commercial colonoscopy simulator, traction of the robot

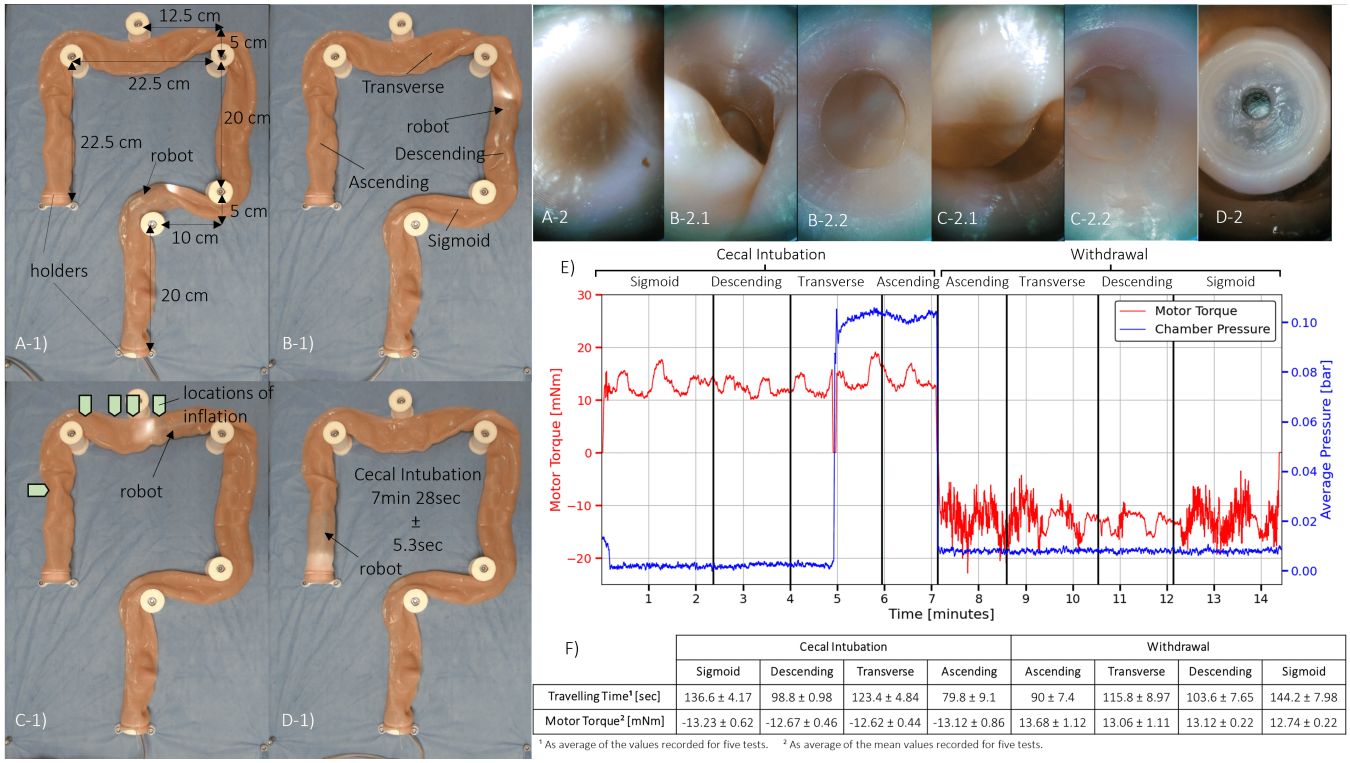

F)

	Cecal Intubation				Withdrawal			
	Sigmoid	Descending	Transverse	Ascending	Ascending	Transverse	Descending	Sigmoid
Travelling Time[1] [sec]	136.6 ± 4.17	98.8 ± 0.98	123.4 ± 4.84	79.8 ± 9.1	90 ± 7.4	115.8 ± 8.97	103.6 ± 7.65	144.2 ± 7.98
Motor Torque[2] [mNm]	-13.23 ± 0.62	-12.67 ± 0.46	-12.62 ± 0.44	-13.12 ± 0.86	13.68 ± 1.12	13.06 ± 1.11	13.12 ± 0.22	12.74 ± 0.22

[1] As average of the values recorded for five tests. [2] As average of the mean values recorded for five tests.

Fig. 6: Testing inside the intestine simulator designed by Finocchiaro *et al.* [24]. A-1: distance between the foam pins used for the configuration of the colon phantom, with the robot in the sigmoid colon. B-1: labels of the colon regions, with the robot in the descending colon. C-1: locations in the intestine where the user has increased the pressure of the chambers to enable further propulsion of the robot, with the robot in the transverse colon. D-1: the robot in the ascending colon completes the cecal intubation of the phantom. From A-2 to D-2: image captured by the front-facing endoscope of the robot with respect to the locations displayed in A-1 to D-1. E: Representation of the motor torque and chamber pressure (as average between the pressure value of the front and rear chamber) measured during one test of simulated colonoscopy inside the colon phantom (negative torque corresponds to the withdrawal motion). The pressure of the chambers is increased when the robot is passing in the transverse colon to augment the propulsion. After completing the cecal intubation, the chambers are deflated and the robot is withdrawn.

is measured inside the transverse colon segment, that presents both circular and triangular folds as shown in Fig. 5-D. The inner diameter of the segment with circular folds measures approximately ø50mm, while it decreases over the segment with triangular haustrae. It is worth mentioning that although the phantom is anatomically realistic internally, it is composed of unexpandable rubber and the prominent anatomy of the flexure of the phantom may affect the locomotion of the robot. The results indicate that the robot can enhance its traction when moving in the segment with circular folds by increasing the chamber pressure. Conversely, within the section with triangular folds, the maximum pulling force exhibits limited increment with the increase of the internal chamber pressure, as shown in Fig. 5-E for the comparison between individual tests, and in Fig. 5-F where the results are shown for the various level of pressure evaluated. The traction reduction is due to the smaller diameter of the triangular-shaped section and the mismatch between the expanded shape of the robot and the external lining, which caused some tracks to produce limited traction or slippage.

G. Silicone simulators testing

This section presents the testing performed inside the intestine simulator designed by Finocchiaro *et al.* [24], which embeds a number of flexures designed based on an intestine CT scan. The phantom was laid and held on a configuration with pins made of foam and screws to mimic the presence of mesentery, as shown in Fig. 6-A-1 to 6-D-1, and internally lubricated with Vaseline. Then, the robot was advanced and withdrawn five times, while the user operated the pressure and speed of the robot arbitrarily via the joystick, relying on the internal (from the on-board endoscope) observation while feeding or withdrawing the cable manually.

For all the tests, the robot succeeded in the cecal intubation and withdrawal throughout the phantom, as shown in Fig. 6-A-1 to 6-D-1, providing image recording of the internal lining of the phantom as shown from Fig. 6-A-2 to 6-D-2. Notably, the imaging of the internal lining can be enhanced by insufflating the phantom with air (by mean of a ø2 mm silicone tube located in the tool canal, while a sliding sealing between a rubber ring and the cable of the robot in the holder at the entrance holds the air in the phantom), as shown in Fig. 6-B-2.2 and 6-C-2.2, that provides expansion of the otherwise collapsed phantom, at the locations shown in Fig. 6-B-1 and 6-C-1. The pressure of the chambers of the robot was occasionally inflated to circa 0.1 bar by the user to increase the propulsion as soon as the robot was observed to stop the advancement during the cecal intubation. During the simulated colonoscopy, the need for inflation occurred in the transverse colon (4 times) and in the ascending colon (1 time), as displayed in Fig. 6-E, where the

results of motor torque and chamber pressure of one test are represented. The results recorded an average time of 7 min and 18 sec ± 5.3 sec for the cecal intubation (thus an average robot speed of 2.8 mm/s), and 7 min and 34 sec ± 18.3 sec for the withdrawal (thus a withdrawal average speed of 2.7 mm/s). The robot repeatedly travels the sections of the colon phantom, as shown in Fig. 6-F, where the time of traveling and the mean of the motor torque are presented for the regions of the phantom (negative torque corresponds to the withdrawal motion). Inside the phantom, the front-facing endoscope of the robot enables the image recording of the internal lining, however, the lack of steering motion of the front-facing camera resulted in unseen areas in the field of vision, in particular at the bends of the phantom.

V. CONCLUSIONS AND DISCUSSION

In this study, we presented a miniaturised version of the SoftSCREEN system for colonoscopy, an active robotic system featured with shape-shifting capability aimed at performing screening and intervention inside the GI tract in a minimally invasive manner. This novel design leverages the use of track-based locomotion with a single embedded motor and adaptive diameter control for the continuous intraluminal locomotion. By monitoring pressure, motor current, and propulsion force, we characterised the expansion of the chambers embedded in the system as a functional means for traction modulation in the lumen, and we demonstrated that the robot successfully maneuvered complex sections resembling the anatomy of the colon with a simple control by the user. The ability to move forward and backward while capturing internal images and the integration of a pathway for the biopsy tool demonstrated its potential for diagnostic and interventional applications inside the intestine. Future work will focus on further miniaturisation, *in vitro* and *ex vivo* testing, the integration of dedicated irrigation channel for both lens and lumen cleaning, and also of an active steering mechanism to enable more controllable imaging of the flexures and tool deployment. In conclusion, we presented promising advancements for the SoftSCREEN system, offering adaptability to various geometries of the human large intestine and enhanced traction force. Further research and development in this direction could pave the way for safer more comfortable procedures for the patient, and more efficient colonoscopy procedures.

References

[1] "WHO/Europe — Cancer."

[2] C. Winters, V. Subramanian, and P. Valdastri, "Robotic, self-propelled, self-steerable, and disposable colonoscopes: Reality or pipe dream? A state of the art review," 9 2022.

[3] A. Alazmani, A. Hood, D. Jayne, A. Neville, and P. Culmer, "Quantitative assessment of colorectal morphology: Implications for robotic colonoscopy," *Medical Engineering Physics*, vol. 38, no. 2, pp. 148–154, 2016.

[4] G. Ciuti, K. Skonieczna-Żydecka, W. Marlicz, V. Iacovacci, H. Liu, D. Stoyanov, A. Arezzo, M. Chiurazzi, E. Toth, H. Thorlacius, P. Dario, and A. Koulaouzidis, "Frontiers of Robotic Colonoscopy: A Comprehensive Review of Robotic Colonoscopes and Technologies," *Journal of Clinical Medicine*, 2020.

[5] L. Manfredi, "Endorobots for Colonoscopy: Design Challenges and Available Technologies," *Frontiers in Robotics and AI*, vol. 8, no. July, pp. 1–10, 2021.

[6] P. Valdastri, G. Ciuti, A. Verbeni, A. Menciassi, P. Dario, A. Arezzo, and M. Morino, "Magnetic air capsule robotic system: Proof of concept of a novel approach for painless colonoscopy," *Surgical Endoscopy*, vol. 26, no. 5, pp. 1238–1246, 2012.

[7] M. Verra, A. Firrincieli, M. Chiurazzi, A. Mariani, G. L. Secco, E. Forcignanò, A. Koulaouzidis, A. Menciassi, P. Dario, G. Ciuti, and A. Arezzo, "Robotic-assisted colonoscopy platform with a magnetically-actuated soft-tethered capsule," *Cancers*, 2020.

[8] G. Pittiglio, L. Barducci, J. W. Martin, J. C. Norton, C. A. Avizzano, K. L. Obstein, P. Valdastri, G. Pittiglio, L. Barducci, J. W. Martin, J. C. Norton, P. Valdastri, and C. A. Avizzano, "Magnetic Levitation for Soft-Tethered Capsule Colonoscopy Actuated With a Single Permanent Magnet: A Dynamic Control Approach," *IEEE ROBOTICS AND AUTOMATION LETTERS*, vol. 4, no. 2, 2019.

[9] Y. Xu, K. Li, G. Student Member, Z. Zhao, and M. Q-H Meng, "Autonomous Magnetic Navigation Framework for Active Wireless Capsule Endoscopy Inspired by Conventional Colonoscopy Procedures; Autonomous Magnetic Navigation Framework for Active Wireless Capsule Endoscopy Inspired by Conventional Colonoscopy Procedures," *IEEE Robotics and Automation Letters*, vol. 7, no. 2, 2022.

[10] J. Zhang, Y. Liu, J. Tian, D. Zhu, and S. Prasad, "Design and Experimental Investigation of a Vibro-Impact Capsule Robot for Colonoscopy," *IEEE Robotics and Automation Letters*, vol. 8, pp. 1842–1849, 3 2023.

[11] G. A. Formosa, J. M. Prendergast, S. A. Edmundowicz, and M. E. Rentschler, "Novel Optimization-Based Design and Surgical Evaluation of a Treaded Robotic Capsule Colonoscope," *IEEE Transactions on Robotics*, vol. 36, no. 2, pp. 545–552, 2020.

[12] F. Fukunaga and J. Y. Nagase, "Cylindrical elastic crawler mechanism for pipe inspection inspired by amoeba locomotion," *Proceedings of the IEEE RAS and EMBS International Conference on Biomedical Robotics and Biomechatronics*, vol. 2016-July, pp. 424–429, 7 2016.

[13] Y. G. e. a. Jianlin Yang, Zhijun Sun, "A Novel Airbag Aided Differential-drive Capsule Robot Towards Colonoscopy,"

[14] J. Norton, A. Hood, A. Neville, D. Jayne, P. Culmer, A. Alazmani, and J. Boyle, "RollerBall: A mobile robot for intraluminal locomotion," *Proceedings of the IEEE RAS and EMBS International Conference on Biomedical Robotics and Biomechatronics*, vol. 2016-July, pp. 254–259, 2016.

[15] J.-Y. Nagase, F. Fukunaga, K. Ogawa, and N. Saga, "Funicular Flexible Crawler for Colonoscopy," *IEEE Transactions on Medical Robotics and Bionics*, vol. 1, pp. 22–29, 1 2019.

[16] K. Osawa, R. Nakadate, J. Arata, Y. Nagao, T. Akahoshi, M. Eto, and M. Hashizume, "Self-Propelled Colonoscopy Robot Using Flexible Paddles," *IEEE Robotics and Automation Letters*, vol. 5, no. 4, pp. 6710–6716, 2020.

[17] D. Lee, S. Joe, J. Choi, B. I. Lee, and B. Kim, "An elastic caterpillar-based self-propelled robotic colonoscope with high safety and mobility," *Mechatronics*, vol. 39, pp. 54–62, 2016.

[18] O. C. Kara, H. Kim, J. Xue, T. G. Mohanraj, Y. Hirata, N. Ikoma, and F. Alambeigi, "Design and development of a novel soft and inflatable tactile sensing balloon for early diagnosis of colorectal cancer polyps," in *2023 IEEE/RSJ International Conference on Intelligent Robots and Systems (IROS)*, pp. 10295–10300, 2023.

[19] L. Manfredi, E. Capoccia, G. Ciuti, and A. Cuschieri, "A Soft Pneumatic Inchworm Double balloon (SPID) for colonoscopy," *Scientific Reports*, vol. 9, no. 1, pp. 1–9, 2019.

[20] J. Ortega Alcaide, Y. Huan, N. Gabrieli, A. Firrincieli, L. Ricotti, P. Dario, and G. Ciuti, "Tether-colon interaction model and tribological characterization for front-wheel driven colonoscopic devices," *Tribology International*, vol. 156, 4 2021.

[21] V. Consumi, L. Lindenroth, J. Merlin, D. Stoyanov, and A. Stilli, "Design and evaluation of the softscreen capsule for colonoscopy," *IEEE Robotics and Automation Letters*, pp. 1–8, 2023.

[22] C. Zhang, H. Liu, R. Tan, and H. Li, "Modeling of velocity-dependent frictional resistance of a capsule robot inside an intestine," *Tribology Letters*, vol. 47, no. 2, pp. 295–301, 2012.

[23] T. L. Pan, M. C. Lei, W. Y. Ng, and Z. Li, "Analytical Modeling of the Interaction Between Soft Balloon-Like Actuators and Soft Tubular Environment for Gastrointestinal Inspection," *Soft Robotics*, vol. 9, pp. 386–398, 4 2022.

[24] M. Finocchiaro, C. Zabban, Y. Huan, A. D. Mazzotta, S. Schostek, A. Casals, A. Hernansanz, A. Menciassi, A. Arezzo, and G. Ciuti, "Physical simulator for colonoscopy: a modular design approach and clinical validation," *IEEE Access*, 2023.